catalysts

MDPI

Article

Synthesis and Visible Light Catalytic Performance of BiOI/Carbon Nanofibers Heterojunction

Kexin Wang [1,2,*], Lina Liu [1], Yongsheng Zhang [1], Jianfeng Su [1], Ruirui Sun [1], Jiao Zhang [1], Yajie Wang [1] and Mingyi Zhang [3,*]

[1] Department of Mathematics and Physics, Luoyang Institute of Science and Technology, Luoyang 471023, China
[2] Henan Province International Joint Laboratory of Materials for Solar Energy Conversion and Lithium Sodium Based Battery, Luoyang Institute of Science and Technology, Luoyang 471023, China
[3] Key Laboratory for Photonic and Electronic Bandgap Materials, Ministry of Education, School of Physics and Electronic Engineering, Harbin Normal University, Harbin 150025, China
* Correspondence: wangkx217@163.com (K.W.); zhangmingyi@hrbnu.edu.cn (M.Z.)

Abstract: Semiconductor materials as photocatalysts hold great prospects for renewable energy substitutes and environmental protection. Nanostructured BiOX (X=Cl, Br, I) with favorable features of a unique layered crystal structure and suitable band gaps has been demonstrated to be a promising photocatalytic material. In this paper, a two-step synthesis route combining an electrospinning technique and SILAR reaction has been accepted as a straightforward protocol for the exploitation of BiOI/carbon nanofibers' (CNFs) hierarchical heterostructures. As expected, the BiOI/CNFs presented a much higher degradation rate of methyl orange than that of the pure BiOI under visible light. The degradation rate of methyl orange reaches 85% within 210 min. The enhanced photocatalytic activity could be attributed to the fact that conductive CNFs as substrate could effectively improve the separation and transformation of photogenerated charges. Moreover, the fabricated BiOI/CNFs after five cycles could be easily recycled without a decrease in photocatalytic activity due to their ultra-long one-dimensional nano-structural property.

Keywords: BiOI; carbon nanofibers; photocatalysts; electrospinning

Citation: Wang, K.; Liu, L.; Zhang, Y.; Su, J.; Sun, R.; Zhang, J.; Wang, Y.; Zhang, M. Synthesis and Visible Light Catalytic Performance of BiOI/Carbon Nanofibers Heterojunction. *Catalysts* **2022**, *12*, 1548. https://doi.org/10.3390/catal12121548

Academic Editor: Da-Ren Hang

Received: 10 October 2022
Accepted: 28 November 2022
Published: 1 December 2022

1. Introduction

Semiconductor photocatalysis provides an effective solution to energy supply and environmental pollution [1]. Since TiO_2 was found to have photocatalytic activity, many photocatalysts have been studied in recent years [2]. As novel semiconductor photocatalysts, bismuth oxyhalides (BiOX, X = Cl, Br, I) have been studied extensively because of their unique properties and potential applications in photocatalysis [3–5]. In particular, bismuth iodide (BiOI) has a bandgap of about 1.8 eV, showing good visible light catalytic activity. [6–8]. However, the photocatalytic performance of BiOI is still affected by disadvantages such as the photogenerated charge carriers and the easy aggregation of nanoparticles [9]. In order to meet practical application, the photocatalytic performance should be further improved. At present, the methods to improve the catalytic performance of BiOI include self-doped iodine [10] and surface modified precious metals such as Ag [11] and Pt [12]. Another method is to form heterojunctions or nanocomplexes with other materials, such as BiOCl/BiOI [13,14], BiOBr/BiOI [15,16], BiOI/TiO_2 [17,18], AgI/BiOI [19,20], BiOI/Bi_2O_3 [21,22] and ZnO/BiOI [23,24], both showing that heterojunctions can effectively improve the light absorption range and promote the separation of photogenerated carriers.

As catalyst carriers in heterojunctions, carbon materials, including bulk carbon materials and nano-carbon materials, have high electrical conductivity, good charge transport capacity, high mechanical strength and stable chemical and physical properties. Bulk carbon materials include activated carbon, carbon black, etc. Nanometer carbon materials

include fullerenes, graphene, carbon nanotubes and carbon nanofibers. As is known, bulk nanomaterials are easy to be recycled and reused, but carbon nanomaterials have better photocatalytic activity than bulk carbon materials due to their nano effect, quantum effect and large specific surface area. The small aspect ratio of zero-dimensional fullerenes and one-dimensional carbon nanotubes is not conducive to recovery [25–29]. Although 2D graphene material has a large aspect ratio, it is easy to curl in practice, which reduces photocatalytic activity and does not use recycling. Therefore, the carbon material used as catalyst support in the construction of heterojunctions should have characteristics both of small size and high specific surface area of nanomaterials and of easy settlement and separation of macroscopic materials.

According to the above analysis, we report a successful attempt for the fabrication of BiOI/CNF hierarchical heterostructures via a simple electrospinning technique and a successive ion layer adsorption reaction (SILAR). The photocatalytic activity of these heterostructures was investigated by measuring the degradation of MO as a test substance. By changing the growth times of BiOI during SILAR, the catalyst load can be adjusted accordingly. In addition, the photocatalytic activity of BiOI/CNFs heterojunction after sedimentation was basically unchanged, showing stable recycling performance [30–33].

The above BiOI/carbon nanofibers' heterojunction system has the following advantages: (1) One-dimensional carbon nanofiber structures with good electron transport ability can effectively separate photogenerated electron hole pairs and improve photocatalytic activity. (2) The carbon nanofibers have favorable recycling characteristics due to their nanofibrous nonwoven structures, which can be easily separated from the solution system by sedimentation without a decrease in photocatalytic activity. (3) The 3D open structures and large surface areas of CNFs provide more active sites for the assembly of secondary BiOI nanostructures with both high density and good dispersion.

2. Result and Discussion

The reaction process is cycled 20 times and the reactant concentration is controlled within a certain range to ensure that the reactant is fully grown on the surface of CNFs. To observe the microtopography of samples, the scanning electron microscopy (SEM) images were detected. As can be seen in Figure 1a,b, as the concentration of the precursor solution increases from 0.125 mM to 0.25 mM, the load on the surface of the CNFs increases significantly and the diameter of the nanosheets increases. This is due to the fact that slightly higher concentrations of the solution can provide sufficient BiO^+ and I^- to generate BiOI. As the concentration continues to rise to 0.5 mM, trace amounts of independent nucleated BiOI nanosheets (Figure 1c) appear in the sample, the concentration continues to rise to 0.75 mM and large BiOI agglomerations appear on the sample surface (Figure 1d). Therefore, a precursor solution concentration of 0.25 mM may be the optimal concentration for the synthesis of BiOI/CNFs.

According to the most suitable precursor reaction solution concentration of 0.25 mM, the nanostructure of BiOI/CNF heterojunction prepared by different cycle growth times of the official production is shown in Figure 2. Since the precursor solution is sprayed by rotation during the electrospinning process, the arrangement of CNFs shown in Figure 2a is random and disordered. As can be seen from the enlarged image, these CNFs have a smooth surface and no secondary structure, with a diameter of about 200 nm. Figure 2b–d show the composite nanofibers after growing BiOI nanosheets on the CNFs' surface. It is observed that the resulting material retained the configuration of the fibers after the SILAR reaction. As the number of continuous SILAR reactions expands from 10 to 30, the loading of BiOI nanosheets grown on the surface of CNFs also increases. As can be seen from the high magnification SEM pattern in the illustration, the diameter of the BiOI nanosheet also gradually increases. The composite nanofibers are about 1 μm in diameter when grown for 30 cycles, which may cause the change in crystallization quality. Notably, BiOI nanosheets grow closely on the surface of CNFs without agglomeration due to the consistency of active growth sites on the CNF surface.

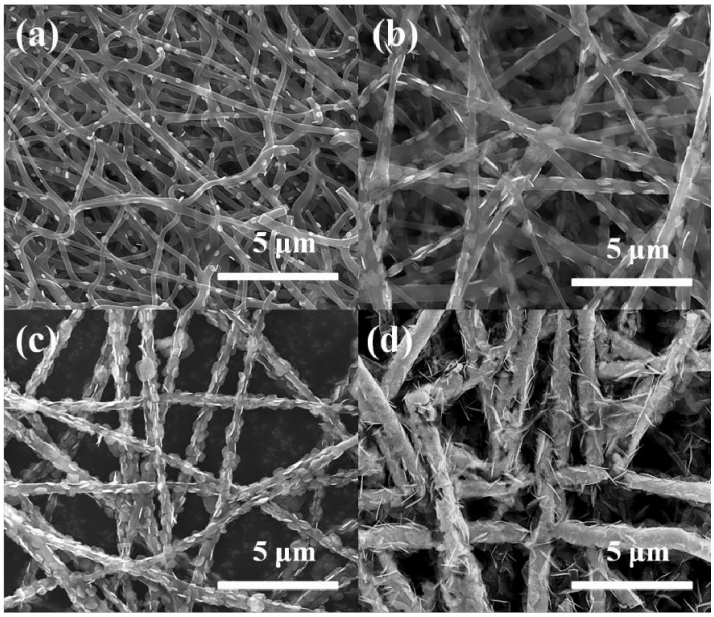

Figure 1. SEM images of BiOI/CNFs with different reaction solution concentrations (**a**) 0.125 mM; (**b**) 0.25 mM; (**c**) 0.5 mM; (**d**) 0.75 mM.

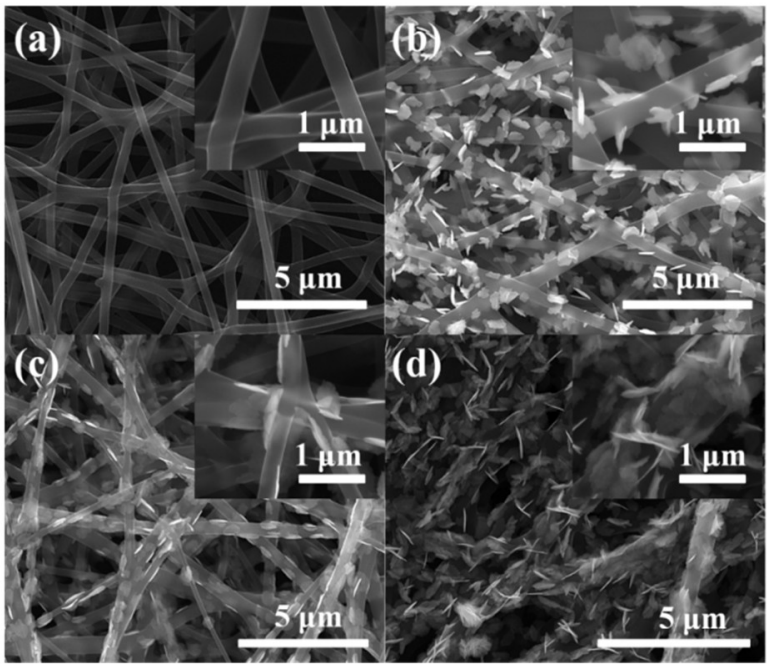

Figure 2. SEM images of (**a**) CNFs, (**b**) BiOI/CNFs-C10, (**c**) BiOI/CNFs-C20 and (**d**) BiOI/CNFs-C30.

Figure 3 has shown the transmission electron microscopy (TEM) and high-magnification transmission electron microscopy (HRTEM) images of the BiOI/CNFs-C30 heterojunction. It can be seen in Figure 3a that a large number of BiOI nanosheets are uniformly surrounded by the surface of the CNFs, which match the SEM images of BiOI/CNF heterojunctions. In Figure 3b, a clear boundary exists between amorphous and crystalline, which proves the successful construct of the heterojunction, where the amorphous part consists of CNFs, while those with distinct lattice diffraction streaks belong to BiOI nanosheets. The lattice spacing of the BiOI nanosheets is 0.28 nm, which corresponds to the (110) atomic surface of its tetragonal crystal form.

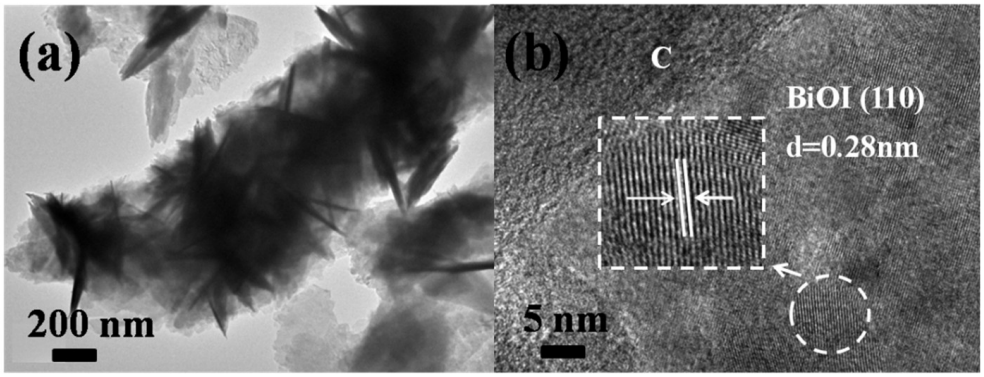

Figure 3. (**a**,**b**) TEM images of and (**c**) HRTEM image of BiOI/CNFs-C30.

Figure 4 shows X-ray diffraction spectra (XRD) of CNFs, BiOI and BiOI/CNFs heterojunctions. The characteristic peak at 24° corresponds to CNFs' (002) atomic plane. In contrast to pure CNFs, in addition to the above peak, a series of special peaks appear at 29.6°, 31.6°, 37.3°, 39.3°, 45.3°, 51.3°, 55.1° of the BiOI/CNFs heterojunctions (solid circles signed). These characteristic peaks correspond to the (102), (110), (112), (004), (200), (114) and (212) surfaces of the tetragonal form BiOI (JCPDS 73-2-62), respectively. The XRD spectral lines of pure BiOI samples also prove the above results. In addition, there are no impurity peaks in all samples, which indicates that the samples are prepared successfully. It can also be observed from the XRD pattern that as the number of continuous reaction cycles increases, from BiOI/CNFs -C10 to BiOI/CNFs-C30, the BiOI loading also gradually increases. The strength of the diffraction peaks of BiOI tends to be sharper and more prominent, which indicates that the crystallinity of BiOI becomes better. According to the above data, the synthesis of the BiOI/CNF heterojunction may promote visible light catalytic activity, while good crystallinity of BiOI will further promote photocatalytic activity.

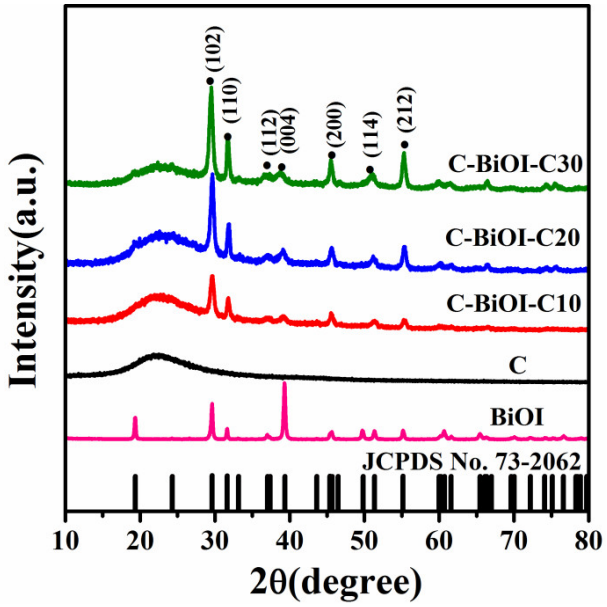

Figure 4. XRD patterns of samples.

To determine the chemical state of each composition in the sample, all the samples are tested by X-ray photoelectron spectroscopy (XPS). Figure 5a shows the full X-ray photoelectron spectra of CNFs and BiOI/CNFs-C30 heterojunctions. There are C, N and O elements in the CNFs. Besides the above elements, the Bi and I elements exist in the BiOI/CNFs-C30 heterojunctions. Element N in both samples may have come from nitrogen during testing. Figure 5b shows the O 1s energy spectrum of CNFs and BiOI/CNFs-C30

heterojunctions. The binding energy of 531.1 eV belongs to I-O bonds in BiOI, and the binding energy of 532.4 eV belongs to surface oxygen adsorption, which is the surface hydroxy group and chemisorbed oxygen. Another characteristic peak of O 1s at a low binding energy of 529 eV in BiOI/CNFs-C30 is caused by lattice oxygen of Bi-O bonds in BiOI, as the energy spectrum of Bi 4F of BiOI/CNFs-C30. The binding energies locate at 158.3 eV and 163.6 eV due to Bi $4F_{7/2}$ and Bi $4F_{5/2}$, respectively, which are derived from the Bi-O bond in BiOI (Figure 5c). The energy spectrum I 3d of BiOI/CNFs-C30 is shown in Figure 5d, with characteristic peaks at 618.2 and 629.7 eV corresponding to I $3d_{3/2}$ and I $3d_{5/2}$, respectively. These results indicate that the composite heterojunction was composed of CNFs and BiOI.

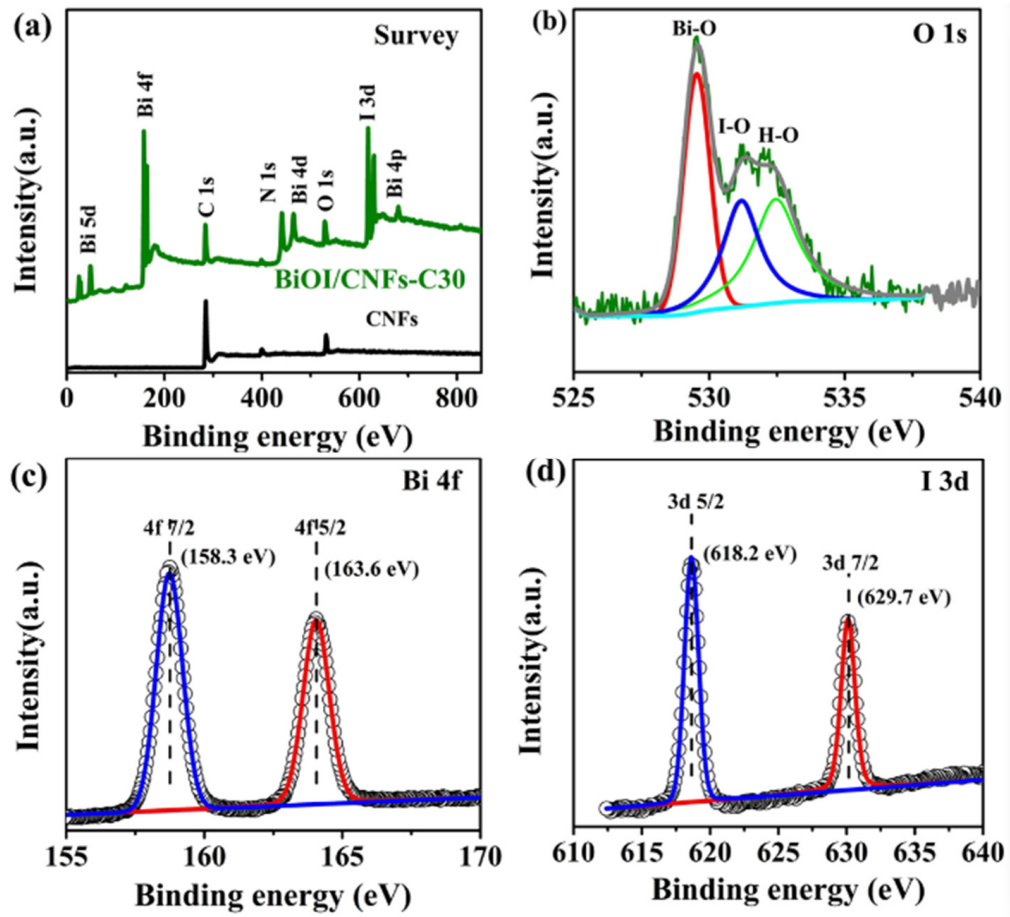

Figure 5. Full XPS spectrum of (**a**) CNFs and BiOI/CNFs-C30, High-resolution XPS spectra of (**b**) O 1s (**c**) Bi 2p and (**d**) I 3d of BiOI/CNFs-C30.

The Fourier transform infrared (FT-IR) spectra of the sample CNFs and BiOI/CNFs-C30 are shown in Figure 6. The vibration peaks located at 1220 cm^{-1}, 1550 cm^{-1} and 3440 cm^{-1} can be attributed to C-C stretching vibration, symmetric and asymmetric COO- stretching vibration and OH- stretching vibration of the sample surface. Compared with CNFs and BiOI/CNFs-C30, the characteristic peak in the low-frequency zone that is less than 1000 cm^{-1} is typical of the Bi=O=Bi vibration of BiOI/CNFs-C30. This result indicated that BiOI nanosheets were successfully compounded on CNFs, which is consistent with the above analysis results.

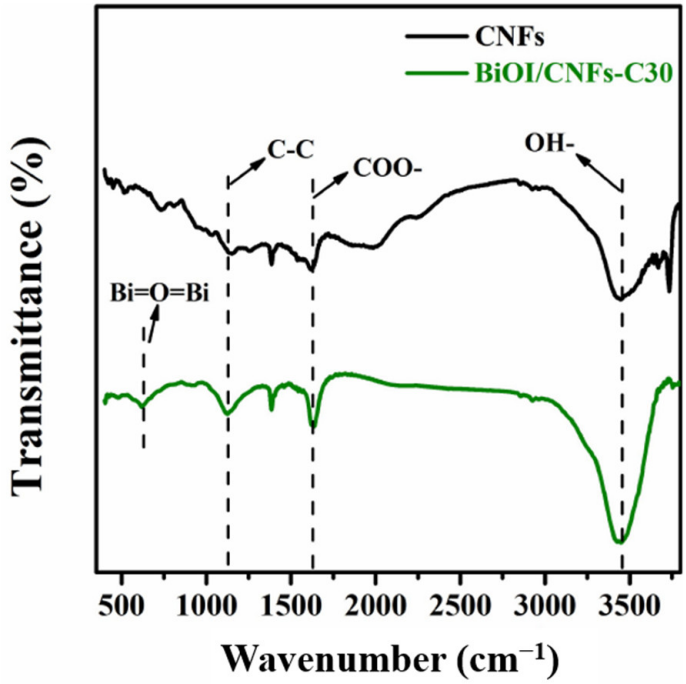

Figure 6. FTIR spectra of CNFs and BiOI/CNFs-C30.

In assessing the photocatalytic activity of the sample by degradation of the MO dye solution under visible light, C and C_0 are the concentrations of MO at a certain time and initial time, respectively, and C/C_0 is the degradation rate. As shown in Figure 7a, the degradation rates of different samples CNFs, BiOI/CNFs-C10, BiOI/CNFs-C20 and BiOI/CNFs-C30 were 11%, 37%, 62% and 85%, respectively. In Figure 7b, the kinetic linear simulation curves show that the above degradation reactions followed a Langmuir–Hinshelwood apparent first-order kinetics model. Due to the low initial concentrations of the reactants, this could be simplified as the following equation:

$$\ln C_0/C = kKt = k_{app}t \quad (1)$$

where C is the concentration (mg/L), t is the visible-light irradiation time, k is the reaction rate constant [mg/(L min)] and K is the adsorption coefficient of the reactant (L/mg). k_{app} is the apparent first-order rate constant (min^{-1}). The order of photocatalytic activity is BiOI/CNFs-C30 > BiOI/CNFs-C20 > BiOI/CNFs-C10, which is consistent with the activity studies above. The photocatalytic activity of BiOI/CNFs-C30 is obviously higher or close to the reported flexible photocatalysts due to the existence of a semiconductor heterojunction to boost the separation of photoinduced charge carriers (Table 1). The degradation of CNFs is caused by the adsorption of the dye molecules by inherent capability. Comparing BiOI/CNFs heterojunction and monomer BiOI powder, it can be seen that the degradation rate of the heterojunction is higher than that of monomer, which is due to CNFs in the heterojunction as electron-trapping substances. CNFs can effectively transfer the photogenerated electrons of BiOI to the surface of the BiOI/CNFs heterojunction for photocatalytic reaction degradation of methyl orange, thereby improving BiOI photocatalytic activity. In addition, the photocatalytic activity of BiOI/CNFs composite nanofibers is related to the amount of BiOI. As the amount of load increases, the photocatalytic activity also increases. This suggests that the number of heterojunctions in BiOI/CNF samples also affects their photocatalytic activity. The control experiment for BiOI/CNFs-C30 was performed in the presence of the photocatalysts, but in the dark. These results show that the adsorption–desorption equilibrium of MO in the dark is established within 30 min (Figure 8).

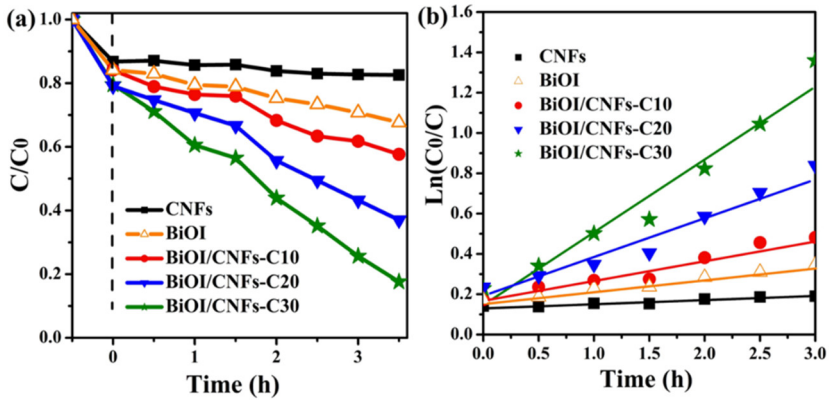

Figure 7. (**a**) Photocatalytic degradation of MO and (**b**) kinetic linear simulation curves over different BiOI/CNFs contents in visible light.

Table 1. The photocatalytic degradation parameters over the different nanofibers photocatalysts.

Photocatalyst	Light	Photocatalytic Results	Year	Refs.
AgI-BiOI/PAN composite nanofibers	300 W Xe lamp (λ > 400 nm)	the photodegradation efficiency of RhB can reach 98.5% at 210 min	2018	[34]
anatase–rutile/BiOI composite fibers	250 W xenon lamp	the degradation rate of MO reaches 54% within 12 h	2022	[35]
TiO_{2-x}/BiOI/AgBr photocatalyst.	500 W xenon lamp (λ ≥ 420 nm)	The RhB, MB and fuchsine are degraded by 98% (60 min), 99% (300 min) and 76% (300 min)	2019	[36]
80%BiOCl/20%BiOI particles	300 W Xe lamp	The degradation efficiency of MO could reach 75.0% after irradiation for 390 min	2012	[37]
PAN/g-C_3N_4/BiOI nanofibers	500 W Xe lamp (λ ≥ 400 nm)	The degradation efficiency of RhB could reach 98.0% after irradiation for 90 min	2018	[38]
ZIF-8@BiOI composites	250 W xenon lamp (λ ≥ 420 nm)	The degradation efficiency of antibiotic tetracycline could reach 86.2% after irradiation for 90 min	2022	[39]
flower-like BiOI	Artificial visible light	the photodegradation efficiency of RhB can reach 100% at 80 min	2021	[40]
BiOI/NH_2-MIL-125(Ti) composite photocatalyst	300 W xenon lamp (λ ≥ 420 nm)	The degradation percentages of Rhodamine B (RhB) and p-chlorophenol (P-CP) reached 99% (240 min) and 90% over BNMT-9 (160 min)	2018	[41]
$Bi_3O_5I_2$ Hollow Microsphere	300-W Xe lamp	81% of MO can be eliminated at 180 min	2019	[42]
flower-like BiOI/BiOCOOH heterojunctions	300 W Xe lamp (λ ≥ 400 nm)	the degradation rate of CIP reaches 87.2% within 125 min	2019	[43]
This work	150 W xenon lamp (λ > 420 nm)	the degradation rate of MO reaches 85% within 210 min		

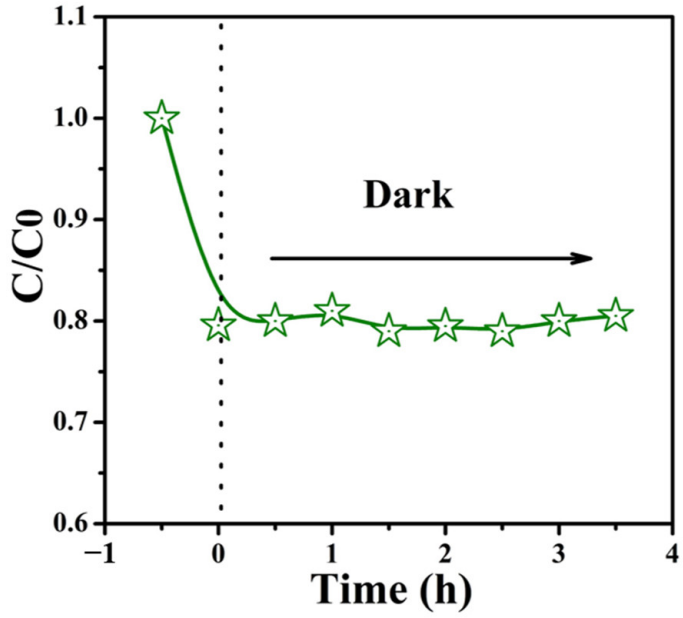

Figure 8. Degradation profiles of MO in the presence of different photocatalysts but in the dark.

To further study the photocatalysis process, ammonium oxalate (AO), Cr(VI), Tert-butyl alcohol (TBA) and benzoquinone (BQ) were, respectively, introduced as the scavengers to quench active holes (h^+), active electron (e^-), hydroxyl radicals (OH) and superoxide radicals (O_2) under visible-light irradiation. As shown in Figure 9 in the presence of AO or Cr(VI), the photodegradation of MO is inhibited remarkably compared with no scavenger at the same conditions. Moreover, the photocatalytic degradation rate also decreases significantly with the addition of BQ. However, after TBA is added into the reaction system, there is almost no change in the photocatalysis property, indicating that the photoelectrons, photogenerated holes and the O_2 all take part in the photocatalytic reactions.

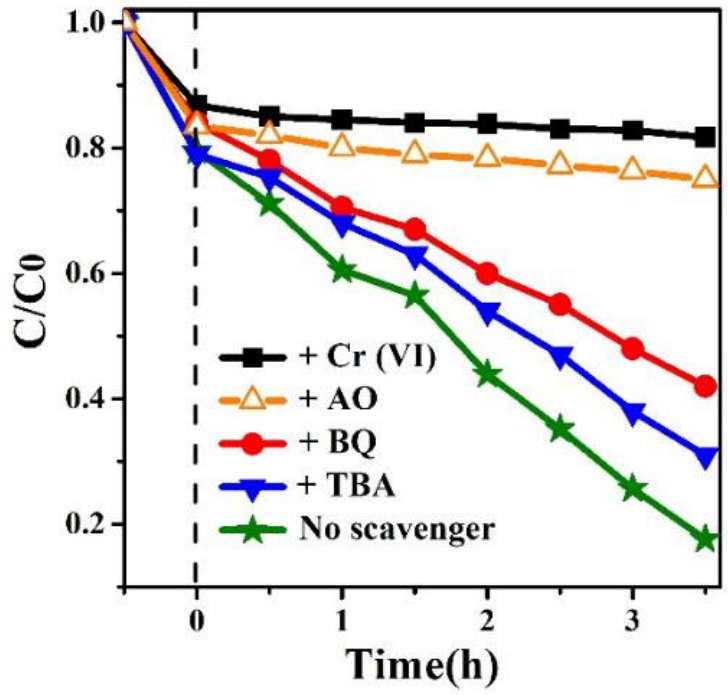

Figure 9. Effect of scavengers on degradation of MO over BiOI/CNFs-30.

According to the above experimental results and discussion, the photocatalytic mechanism of BiOI/CNFs composite nanofibers is shown in Figure 10. As a photocatalyst, CNFs and BiOI nanosheets have synergistic effects in BiOI/CNFs. The visible light catalytic degradation of MO by composite nanofibers is as follows:

$$BiOI + h\upsilon \rightarrow BiOI(e_{cb}^{-} - h_{vb}^{+}) \quad (2)$$

$$e_{cb}^{-} + C\ NFs \rightarrow C\ NFs(e_{cb}^{-}) \quad (3)$$

$$C\ NFs(e_{cb}^{-}) + O_2 \rightarrow O_2\bullet \quad (4)$$

$$O_2\bullet + H_2O \rightarrow HO_2\bullet + OH^{-} \quad (5)$$

$$HO_2\bullet + H_2O \rightarrow H_2O_2 + OH\bullet \quad (6)$$

$$H_2O_2 \rightarrow 2\ OH\bullet \quad (7)$$

$$OH\bullet + MO \rightarrow CO_2 + H_2O \quad (8)$$

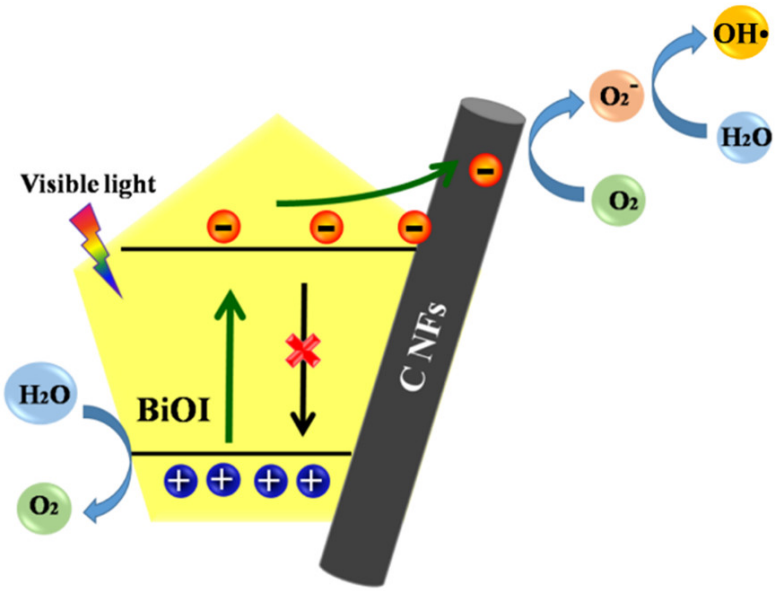

Figure 10. Schematic diagram of the photocatalytic mechanism of BiOI/CNFs.

In order to further study the stability of the prepared catalyst, five cycle experiments were carried out on BiOI/CNFs-C30 catalyst under the same experimental conditions, as shown in Figure 10. It can be seen that the catalytic activity of BiOI/CNFs-C30 basically did not change after five cycles (Figure 11). This indicates that BiOI/CNFs nanofibers has shown excellent performance in the cycling test. At the same time, the one-dimensional ultra-long aspect ratio of the composite nanofiber can be easily separated from the solution after precipitation. In order to investigate the stability of the samples, we tested the SEM and XRD of the samples after cycling. The results show that there is no obvious change in the morphology of the samples after cycling and XRD also shows no change in the structure of the samples. The above results show that the sample prepared in this paper has good stability (Figure 12).

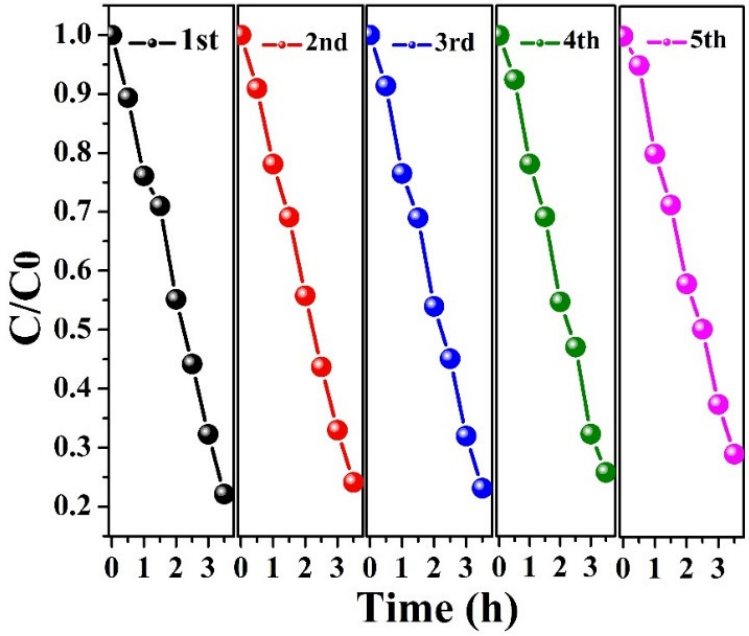

Figure 11. Photocatalytic degradation cycling tests over BiOI/CNFs-C30.

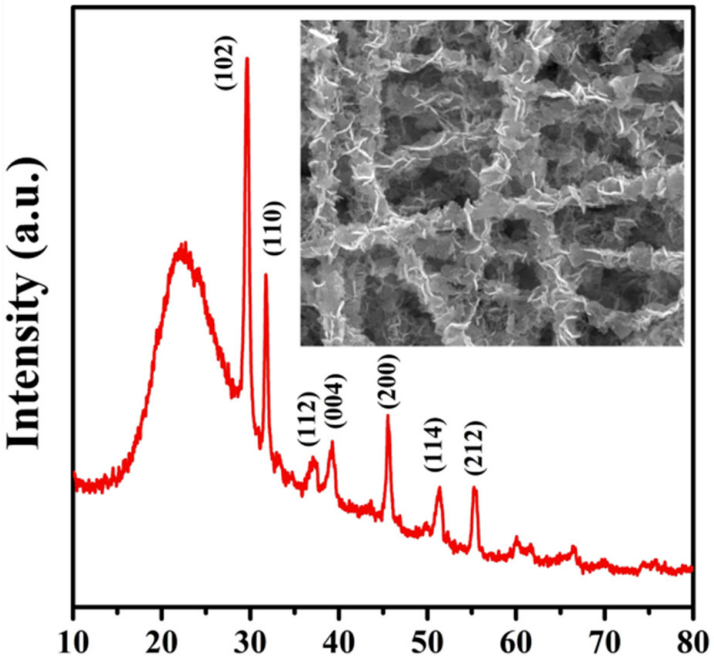

Figure 12. XRD patterns and SEM images (inside) of the BiOI/CNFs-C30 catalyst after the photocatalytic reaction.

3. Materials and Methods

3.1. Preparation of BiOI/CNFs Heterojunction Composite Nanofibers

First, 1.5 g PAN powder (molecular weight 6000) was dissolved in 10 mL N,N-dimethylformamide (DMF) solution and stirred overnight with a magnetic stirrer until the solution is clear. The clarified precursor solution was added to a syringe with a steel needle tip, the needle was ~15 cm away from the aluminum foil receiving plate and a high voltage static electricity of ~12 kV was applied to the needle. After a while, PAN nanofiber was obtained from aluminum foil. The PAN nanofiber was calcined in a tubular furnace and the calcination was maintained at a rate of 1 °C/min to 270 °C for 1 h. Then they were carbonized in nitrogen at 1000 °C at a ramp rate of 5 °C/min and finally cooled

to room temperature. Thus, electro-spun carbon nanofibers (CNFs) were obtained. The CNFs were added to concentrated nitric acid and soaked for 48 h to expose the surface functional groups. After that, the activated CNFs were washed with deionized water to a neutral state.

Secondly, 0.25 mM $Bi(NO_3)_3 \cdot 5H_2O$ and KI solutions were prepared as solution A and solution B, respectively. Each successive ionic layer adsorption and reaction (SILAR reaction) consists of the following four steps: (1) Immersing CNFs into solution A to adsorb BiO^+ ions; (2) Wash off the loose ions adsorbed on the surface with deionizing water; (3) Immerse in solution B to adsorb I^- ions and react with BiO^+ ions; (4) The unreacted ions and loosely immobilized BiOI were washed away by deionizing water, as shown in Figure 1 of the synthesis process. The samples were then cleaned with deionized water and ethanol and dried in an oven at 60 °C. The cycle times of continuous ion layer adsorption reactions are 10, 20 and 30, respectively, which are named BiOI/PAN-C10, BiOI/PAN-C20 and BiOI/PAN-C30. Samples with the same number of reaction cycles and different concentrations of precursor solution were prepared by the same method. The number of cycles was fixed as 20 times and the concentrations of $Bi(NO_3)_3 \cdot 5H_2O$ and KI in the precursor solution were 0.125 mM, 0.25 mM, 0.5 mM and 0.75 mM.

3.2. Characterizing Instruments

Scanning electron microscopy (SEM; Quanta 250 FEG, FEI, Hillsboro, OR, USA) and transmission electron microscopy (TEM; JEOL JEM-2100, JEOL, Tokyo, Japan) were used to characterize the morphology of the samples. X-ray diffraction (XRD, D/Max 2500, Rigaku, Tokyo, Japan), Cu Kα (0.1541 nm); X-ray photoelectron spectroscopy (XPS, VG-Escalab LKII Instrument, VG, Waltham, UK), Mg KADES (hυ = 1253.6 eV), pressure less than 8–10 Pa; Thermogravimetric analysis (TG, NETZSCH STA 449C, atmosphere); UV-Visible diffuse reflection (UH4150, Hitachi, Tokyo, Japan).

3.3. Photocatalytic Test

Methyl orange (MO) was used as a simulated pollutant in the photocatalytic experiments. The photocatalyst (0.1 g) was dispersed in different dye solutions (100 mL, 10 mg/L). In order to achieve adsorption and desorption equilibrium between the catalyst surface and dye molecules, the mixed solution was placed in the dark for 1 h. The filter ($\geq$420 nm) was placed under a xenon lamp at 150 W as a light source for photocatalytic visible light and 4 mL of the reaction solution was drawn every 30 min for analysis. The concentration of reaction solution was obtained by analyzing the absorption peaks of MO reaction solutions at 553 nm using a UH4150 UV-visible diffuse reflectometer.

4. Conclusions

BiOI/C heterojunction composite nanofibers were successfully prepared by combining electrospinning technology with SILAR reaction. The content of BiOI in composite nanofibers was changed by adjusting the cycle growth times of continuous ion layer adsorption reaction. Photocatalytic experiments showed that BiOI/CNFs have enhanced photocatalytic activity compared with BiOI and CNFs when MO was degraded by visible light. With the increase of BiOI content, the photocatalytic properties showed a trend of increasing first and then decreasing. The enhanced photocatalytic activity may be attributed to the extended absorption in the visible light region due to the BiOI nanosheets and the effective separation of the photogenerated carriers driven by the photoinduced potential difference produced at the BiOI-CNF heterojunction interface. The thickening of BiOI shell increases the transport distance of photogenerated carriers and finally leads to the catalytic reaction of photogenerated carriers in the composite heterojunction instead of transporting them to the surface. In addition, BiOI/CNFs are recycled several times due to their special structure while maintaining catalytic activity in the liquid phase.

Author Contributions: Conceptualization, K.W. and M.Z.; methodology, L.L.; software, Y.Z.; validation, J.S.; formal analysis, R.S.; investigation, J.Z.; resources, Y.W.; data curation, K.W.; writing—original draft preparation, K.W.; writing—review and editing, K.W.; visualization, L.L.; supervision, K.W. and M.Z. All authors have read and agreed to the published version of the manuscript.

Funding: Supported by the National Natural Science Foundation of China (Grant No. 11905096), the Natural Science Foundation of Henan Province (Grant Nos. 19A430020, 212102210312, 222300420241, 22A430030, 222300420240, 21A140017, 21A140016, 222102240114, 23B140015).

Data Availability Statement: Not applicable.

Conflicts of Interest: The authors declare no conflict of interest.

References

1. Borgarello, E.; Kiwi, J.; Pelizzetti, E.; Visca, M.; Graetzel, M. Photochemical cleavage of water by photocatalysis. *Nature* **1981**, *289*, 158–160. [CrossRef]
2. Fujishima, A.; Honda, K. Electrochemical Photolysis of Water at a Semiconductor Electrode. *Nature* **1972**, *238*, 37–38. [CrossRef] [PubMed]
3. Mahmoodi, V.; Ahmadpour, A.; Bastami, T.R.; Mousavian, M.T.H. Facile Synthesis of BiOI Nanoparticles at Room Temperature and Evaluation of their Photoactivity Under Sunlight Irradiation. *Photochem. Photobiol.* **2018**, *94*, 4–16. [CrossRef] [PubMed]
4. Luévano-Hipólito, E.; Torres-Martínez, L.M.; Cantú-Castro, L.V.F. Self-cleaning coatings based on fly ash and bismuth-photocatalysts: Bi_2O_3, $Bi_2O_2CO_3$, BiOI, $BiVO_4$, $BiPO_4$. *Constr. Build. Mater.* **2019**, *220*, 206–213. [CrossRef]
5. Xiao, X.; Zhang, W.D. Facile synthesis of nanostructured BiOI microspheres with high visible light-induced photocatalytic activity. *J. Mater. Chem.* **2010**, *20*, 5866–5870. [CrossRef]
6. Peng, Y.; Zhang, Q.; Kan, P.F. Synthesis of a Novel One-dimensional $Bi_2O_2CO_3$–BiOCl Heterostructure and its Enhanced Photocatalytic Activity. *CrystEngComm* **2020**, *22*, 6822–6830. [CrossRef]
7. Arumugam, M.; Choi, M.Y. Recent Progress on Bismuth Oxyiodide (BiOI) Photocatalyst for Environmental Remediation. *J. Ind. Eng. Chem.* **2020**, *81*, 237–268. [CrossRef]
8. Zhong, S.; Zhou, H.; Shen, M.; Yao, Y.; Gao, Q. Rationally Designed a g-C_3N_4/BiOI/$Bi_2O_2CO_3$ Composite with Promoted Photocatalytic Activity. *J. Alloys Compd.* **2021**, *853*, 157307. [CrossRef]
9. Wang, S.; Wang, L.; Huang, W. Bismuth-Based Photocatalysts for Solar Energy Conversion. *J. Mater. Chem. A* **2020**, *8*, 24307–24352. [CrossRef]
10. Zhang, X.; Zhang, L. Electronic and Band Structure Tuning of Ternary Semiconductor Photocatalysts by Self Doping: The Case of BiOI. *J. Phys. Chem. C* **2010**, *114*, 18198–18206. [CrossRef]
11. Cao, J.; Zhao, Y.; Lin, H. Facile synthesis of novel Ag/AgI/BiOI Composites with Highly Enhanced Visible Light Photocatalytic Performances. *J. Solid State Chem.* **2013**, *206*, 38–44. [CrossRef]
12. Yu, C.; Yu, J.C.; Fan, C. Synthesis and Characterization of Pt/BiOIN Catalyst with Enhanced Activity under Visible Light Irradiation. *Mater. Sci. Eng. B Solid-State Mater. Adv. Technol.* **2010**, *166*, 213–219. [CrossRef]
13. Huang, H.; Xiao, K.; He, Y.; Zhang, T.; Dong, F.; Du, X.; Zhang, Y. In Situ Assembly of BiOI@$Bi_{12}O_{17}C_{l2}$ p-n junction: Charge Induced Unique Front-Lateral Surfaces Coupling Heterostructure with High Exposure of BiOI 001 Active Facets for Robust and Nonselective Photocatalysis. *Appl. Catal. B* **2016**, *199*, 75–86. [CrossRef]
14. Xiao, X.; Hao, R.; Liang, M.; Zuo, X.; Nan, J.; Li, L.; Zhang, W. One-pot Solvothermal Synthesis of Three-dimensional (3d) BiOI/BiOCl Composites with Enhanced Visible-light Photocatalytic Activities for the Degradation of Bisphenol-a. *J. Hazard. Mater.* **2012**, *233–234*, 122–130. [CrossRef] [PubMed]
15. Jia, Z.; Wang, F.; Xin, F.; Zhang, B. Simple Solvothermal Routes to Synthesize 3d $BiOBr_xI_{1-x}$ Microspheres and Their Visible-Light-Induced Photocatalytic Properties. *Ind. Eng. Chem. Res.* **2011**, *50*, 6688–6694. [CrossRef]
16. Cao, J.; Xu, B.Y.; Lin, H.L.; Luo, B.D.; Chen, S.F. Chemical Etching Preparation of BiOI/BiOBr Heterostructures with Enhanced Photocatalytic Properties for Organic Dye Removal. *Chem. Eng. J.* **2012**, *185*, 91–99. [CrossRef]
17. Qu, Z.; Su, Y.; Sun, L.; Liang, F.; Zhang, G. Study of the Structure, Electronic and Optical Properties of BiOI/Rutile-TiO_2 Heterojunction by the First-Principle Calculation. *Materials* **2020**, *13*, 323. [CrossRef]
18. Henríquez, A.; Romero, R.; Cornejo-Ponce, L.; Salazar, C.; Díaz, J.; Melín, V.; Mansilla, H.D.; Pecchi, G.; Contreras, D. Selective Oxofunctionalization of Cyclohexane and Benzyl Alcohol over BiOI/TiO_2 Heterojunction. *Catalysts* **2022**, *12*, 318. [CrossRef]
19. Cheng, H.; Huang, B.; Dai, Y.; Qin, X.; Zhang, X. One-step Synthesis of the Nanostructured AgI/BiOI Composites with Highly Enhanced Visible-light Photocatalytic Performances. *Langmuir* **2010**, *26*, 6618–6624. [CrossRef]
20. Cheng, H.; Wang, W.; Huang, B.; Wang, Z.; Zhan, J.; Qin, X.; Zhang, X.; Dai, Y. Tailoring AgI Nanoparticles for the Assembly of AgI/BiOI Hierarchical Hybrids with Size-dependent Photocatalytic Activities. *J. Mater. Chem. A* **2013**, *1*, 7131. [CrossRef]
21. Qin, H.M.; Wang, K.; Jiang, L.S.; Li, J.; Wu, X.Y.; Zhang, G.K. Ultrasonic-assisted Fabrication of a Direct Z-scheme BiOI/Bi_2O_4, Heterojunction with Superior Visible Light-responsive Photocatalytic Performance. *J. Alloys Compd.* **2020**, *821*, 153417. [CrossRef]
22. Yan, Q.; Xie, X.; Liu, Y.; Wang, S.; Zhang, M.; Chen, Y.; Si, Y. Constructing a New Z-scheme Multi-heterojunction Photocataslyts Ag-AgI/BiOI-Bi_2O_3 with Enhanced Photocatalytic Activity. *J. Hazard. Mater.* **2019**, *371*, 304–315. [CrossRef] [PubMed]

23. Tang, J.K.; Xue, Y.F.; Ma, C.L.; Zhang, S.J.; Li, Q.L. Facile Preparation of BiOI/T-ZnOw p–n Heterojunction Photocatalysts with Enhanced Removal Efficiency for Rhodamine B and Oxytetracycline. *New J. Chem.* **2022**, *46*, 13010–13020. [CrossRef]
24. Jiang, J.; Zhang, X.; Sun, P.B.; Zhang, L.Z. ZnO/BiOI Heterostructures: Photoinduced Charge Transfer Property and Enhanced Visible Light Photocatalytic Activity. *J. Phys. Chem. C* **2011**, *115*, 20555–20564. [CrossRef]
25. Aftab, F.; Duran, H.; Kirchhoff, K.; Zaheer, M.; Iqbal, B.; Saleem, M.; Arshad, S.N. A Facile Synthesis of FeCo Nanoparticles Encapsulated in Hierarchical N-Doped Carbon Nanotube/Nanofiber Hybrids for Overall Water Splitting. *ChemCatChem* **2020**, *12*, 932–943. [CrossRef]
26. Li, Y.B.; Zhang, H.M.; Liu, P.R.; Wang, D.; Li, Y.; Zhao, H.J. Cross-linked g-C_3N_4/rGO Nanocomposites with Tunable Band Structure and Enhanced Visible Light Photocatalytic Activity. *Small* **2013**, *9*, 3336–3344. [CrossRef]
27. Hou, Y.; Wen, Z.; Cui, S.; Guo, X.; Chen, J. Constructing 2d Porous Graphitic C_3N_4 Nanosheets/Nitrogen-doped Graphene/layered MoS2 Ternary Nanojunction with Enhanced Photoelectrochemical Activity. *Adv. Mater.* **2013**, *25*, 6291–6297. [CrossRef]
28. Hassanzadeh-Aghdam, M.K.; Mahmoodi, M.J.; Ansari, R. Creep Performance of CNT Polymer Nanocomposites—An Emphasis on Viscoelastic interphase and CNT Agglomeration. *Compos. B Eng.* **2019**, *168*, 274–281. [CrossRef]
29. Atif, R.; Inam, F. Reasons and Remedies for the Agglomeration of Multilayered Graphene and Carbon Nanotubes in Polymers. *Beilstein J. Nanotechnol.* **2016**, *7*, 1174–1196. [CrossRef]
30. Zhou, X.J.; Shao, C.L.; Li, X.H.; Wang, X.X.; Guo, X.H.; Liu, Y.C. Three Dimensional Hierarchical Heterostructures of g-C_3N_4 Nanosheets/TiO_2 Nanofibers: Controllable Growth via Gas-solid Reaction and Enhanced Photocatalytic Activity under Visible Light. *J. Hazard. Mater.* **2018**, *344*, 113–122. [CrossRef]
31. Zhang, J.; Shao, C.L.; Li, X.H.; Xin, J.Y.; Yang, S.; Liu, Y.C. Electrospun $CuAl_2O_4$ Hollow Nanofibers as Visible Light Photocatalyst with Enhanced Activity and Excellent Stability under Acid and Alkali Conditions. *CrystEngComm* **2018**, *20*, 312–322. [CrossRef]
32. Zhang, M.Y.; Qi, Y.; Zhang, Z.Y. AgBr/BiOBr Nano-Heterostructure-Decorated Polyacrylonitrile Nanofibers: A Recyclable High-Performance Photocatalyst for Dye Degradation under Visible-Light Irradiation. *Polymers* **2019**, *11*, 1718. [CrossRef] [PubMed]
33. Sun, Y.C.; Shao, C.L.; Li, X.H.; Guo, X.H.; Zhou, X.J.; Li, X.W.; Liu, Y.C. Hierarchical Heterostructures of p-type bismuth Oxychloride Nanosheets on n-type Zinc Ferrite Electrospun Nanofibers with Enhanced Visible-light Photocatalytic Activities and Magnetic Separation Properties. *J. Colloid Interface Sci.* **2018**, *516*, 110–120. [CrossRef] [PubMed]
34. Zhang, Q.Y.; Bai, J.; Liang, H.O.; Li, C.P. Synthesis of the novel nanostructured AgI-BiOI/PAN composite photocatalyst with highly enhanced visible-light catalytic performances. *J. Photochem. Photobiol. A Chem.* **2018**, *357*, 132–139. [CrossRef]
35. Li, D.; Xu, K.; Zhang, C. Improvement of Photocatalytic Performance by Building Multiple Heterojunction Structures of Anatase–Rutile/BiOI Composite Fibers. *Nanomaterials* **2022**, *12*, 3906. [CrossRef]
36. Sedaghati, N.; Habibi-Yangjeh, A.; Pirhashemi, M.; Vadivel, S. Boosted visible-light photocatalytic performance of TiO_{2-x} decorated by BiOI and AgBr nanoparticles. *J. Photochem. Photobiol. A* **2019**, *384*, 112066. [CrossRef]
37. Luo, B.; Wu, C.; Zhang, F.; Wang, T.; Yao, Y. Preparation of Porous Ellipsoidal Bismuth Oxyhalide Microspheres and Their Photocatalytic Performances. *Materials* **2022**, *15*, 6035. [CrossRef]
38. Zhou, X.J.; Shao, C.L.; Yang, S.; Li, X.W.; Guo, X.H.; Wang, X.X.; Li, X.H.; Liu, Y.C. Heterojunction of g-C_3N_4/BiOI Immobilized on Flexible Electrospun Polyacrylonitrile Nanofibers: Facile Preparation and Enhanced Visible Photocatalytic Activity for Floating Photocatalysis. *ACS Sustain. Chem. Eng.* **2018**, *6*, 2316–2323. [CrossRef]
39. Tang, J.; Duan, Z.; Xu, Q.; Li, C.; Hou, D.; Gao, G.; Luo, W.; Wang, Y.; Zhu, Y. ZnO@Bi_5O_7I Heterojunction Derived fromZIF-8@BiOI for Enhanced Photocatalytic Activity under Visible Light. *Materials* **2022**, *15*, 508. [CrossRef]
40. Narenuch, T.; Senasu, T.; Chankhanittha, T.; Nanan, S. Sunlight-Active BiOI Photocatalyst as an Efficient Adsorbent for the Removal of Organic Dyes and Antibiotics from Aqueous Solutions. *Molecules* **2021**, *26*, 5624. [CrossRef]
41. Du, J.; Zhang, J.; Yang, T.; Liu, R.; Li, Z.; Wang, D.; Zhou, T.; Liu, Y.; Liu, C.; Che, G. The Research on the Construction and the Photocatalytic Performance of BiOI/NH_2-MIL-125(Ti) Composite. *Catalysts* **2021**, *11*, 24. [CrossRef]
42. Cui, B.; Cui, H.; Li, Z.; Dong, H.; Li, X.; Zhao, L.; Wang, J. Novel $Bi_3O_5I_2$ Hollow Microsphere and Its Enhanced Photocatalytic Activity. *Catalysts* **2019**, *9*, 709. [CrossRef]
43. Li, S.; Xue, B.; Wang, C.; Jiang, W.; Hu, S.; Liu, Y.; Wang, H.; Liu, J. Facile Fabrication of Flower-Like BiOI/BiOCOOH p–n Heterojunctions for Highly Efficient Visible-Light-Driven Photocatalytic Removal of Harmful Antibiotics. *Nanomaterials* **2019**, *9*, 1571. [CrossRef] [PubMed]